PAPER • OPEN ACCESS

Coherent control of extreme ultraviolet emission generated through frustrated tunneling ionization

To cite this article: Yang Hwan Kim *et al* 2022 *New J. Phys.* **24** 083002

New Journal of Physics
The open access journal at the forefront of physics

Deutsche Physikalische Gesellschaft DPG
IOP Institute of Physics

Published in partnership with: Deutsche Physikalische Gesellschaft and the Institute of Physics

OPEN ACCESS

RECEIVED
23 March 2022

REVISED
30 June 2022

ACCEPTED FOR PUBLICATION
18 July 2022

PUBLISHED
9 August 2022

PAPER

Coherent control of extreme ultraviolet emission generated through frustrated tunneling ionization

Yang Hwan Kim[1,2], Hyeok Yun[1,3], Sung In Hwang[1], Igor A Ivanov[1], Chang Hee Nam[1,2] and Kyung Taec Kim[1,2,*]

[1] Center for Relativistic Laser Science, Institute for Basic Science, Gwangju 61005, Republic of Korea
[2] Department of Physics and Photon Science, Gwangju Institute of Science and Technology, Gwangju 61005, Republic of Korea
[3] Advanced Photonics Research Institute, Gwangju Institute of Science and Technology, Gwangju 61005, Republic of Korea
[*] Author to whom any correspondence should be addressed.

E-mail: kyungtaec@gist.ac.kr

Keywords: frustrated tunneling ionization, high harmonic generation, strong field physics, attosecond science, EUV emission

Abstract

Coherent extreme ultraviolet (EUV) line emissions can be generated from an atom excited through frustrated tunneling ionization (FTI). The phase variation of the EUV emission in a generation medium along the propagation direction is a critical parameter that determines the phase-matching condition of this new light source. Here we show that the EUV emission sensitively depends on the intensity and phase of a driving laser pulse and the target position. Angle-resolved EUV spectra measured at different target positions and the carrier-envelope phases of the laser pulse exhibit an intensity modulation, showing similar behavior to that of a long-trajectory high harmonic radiation. The four-step model developed for the FTI emission accurately describes the coherent control of the EUV emission. These findings are essential ingredients for developing coherent extreme ultraviolet sources with high photon flux and for utilizing the FTI emission in time-resolved spectroscopy.

1. Introduction

A nonlinear emission resulting from the ultrafast electron dynamics such as high harmonic generation (HHG) sensitively depends on the amplitude and phase of a driving laser field. From the first observation of HHG [1, 2], considerable efforts have been made to understand and control these dependencies [3–9]. This coherent control has enabled phase-matching of HHG [10–15], spatio-temporal measurement and control [16, 17], and high harmonic spectroscopy [18–21].

Recent experiments [22] have demonstrated that a coherent EUV emission can be generated through frustrated tunneling ionization (FTI) followed by free induction decay [23–25]. Since the coherent EUV emission generated through FTI (FTI emission hereafter) also accompanies the tunneling of an electron in an intense laser field and the excursion of the electron near the parent ion, it is expected that the amplitude and phase of the FTI emission can also be sensitively dependent on the driving laser field [7, 8]. However, the phase property of the FTI emission has not been studied much so far.

In this work, we demonstrate that the FTI emission can be coherently controlled using a few-cycle laser field. We use the four-step model that accurately describes the generation mechanism of the FTI emission. It is shown that the amplitude and phase of the FTI emission sensitively depend on the amplitude and phase of the driving laser field. The FTI emission exhibits an intensity modulation when the target position or the carrier-envelope-phase (CEP) of the driving laser field is changed. It is shown that the slow intensity variation of the FTI emission obtained at different target positions is caused by the Gouy phase and the intensity variations of the driving laser field. The fast intensity modulation of the FTI emission is caused by the interference of the electron wave packets originating from the multiple half cycles of the driving laser field. Understanding this behavior is critical to achieving the phase-matching condition of the FTI emission.

2. Method

2.1. Four-step model of FTI emission

Coherent EUV radiation can be emitted through HHG when an atom is exposed to an intense laser field. The semi-classical three-step model describes well the process of HHG [4, 6]. Firstly, a bound electron of the atom is freed by tunneling through the atomic potential deformed by the laser field. Secondly, the electron is accelerated after the tunneling. The electron trajectory is determined by its birth time [26]. Some electron paths allow the electron to return to the parent ion. Finally, the coherent EUV or x-ray radiation is emitted when the electron recombines with the parent ion. This simple three-step model provides an intuitive description of HHG, yet it is sufficiently precise. It has been successfully and widely used in many applications [26].

Coherent EUV radiation can also be emitted through FTI. Similar to HHG, the FTI emission can be explained by the four-step process, as shown in figure 1(a). Firstly, an electron is tunneled out in an intense laser field. Secondly, it oscillates along with the driving laser field. If the electron is ionized at the peak of the electric field, it does not recombine with the parent atom immediately, and it is not driven away after the pulse. This electron is left near the parent atom with near-zero kinetic energy when the laser field is turned off. Thirdly, the electron recombines to the excited state of the parent atom [27]. Finally, the EUV emission is generated through free induction decay. This four-step model also well describes the fundamental property of the FTI emission, as we show below.

Both HHG and FTI emissions are accompanied by the tunneling of an electron and its excursion near the parent ion. Therefore, they share similar properties, such as ellipticity dependence and lighthouse effects [22]. One of the main differences between the two processes, however, is the timing of recombination and light emission mechanism. HHG occurs when the tunnel-ionized electron recombines within around a half-optical cycle (short trajectories) or one optical cycle (long trajectories) [4]. On the other hand, electrons tunneled out at the crests of multiple half-optical cycles recombine at the end of the laser field in the case of the FTI emission, as shown in figure 1(a). Therefore, the amplitude and the phase of the emissions can be described in a slightly different way.

2.2. Phase of FTI emission calculated using the four-step model

To investigate the phase dependence of the FTI emission on a driving laser field, we calculated the phase of the FTI emission generated from a single atom using the four-step model numerically near the focus [27]. In the four-step model, the phase of the FTI emission accumulated along the electron trajectories was calculated as $\phi_{\mathrm{FTI}} = I_{\mathrm{p}} t_{\mathrm{i}} - \int_{t_{\mathrm{i}}}^{t_{\mathrm{R}}} v^2/2 \, \mathrm{d}t$ in atomic units. Here, I_{p} is the ionization potential of a target atom. t_{i} and t_{R} are ionization time and recombination time, respectively. v is the mechanical momentum of the electron. The amplitude of the FTI emission was determined by an ionization rate at t_{i} obtained using the ADK ionization model [28].

The intensity and the phase of the laser field vary near the focus, as shown in figures 1(b) and (c). For the sake of simplicity, the phase of the FTI emission for different Gouy phases ($\phi^{\mathrm{G}}_{\mathrm{FTI}}$, blue solid line) and for intensity variation ($\phi^{\mathrm{I}}_{\mathrm{FTI}}$, red solid line) are calculated separately for a single electron trajectory (i.e. the trajectory shown with a yellow dashed line in figure 1(a)) in which tunneling occurs at the peak ($t = 0$) of the laser field, as shown in figure 1(d). When these two effects are considered (yellow solid line in figure 1(d)), the phase of the FTI emission decreases with a large slope before the focus ($z < 0$). The phase of the FTI emission is flat right after the focus (near $z = 2.5$ mm) because the phase variation caused by the Gouy phase and intensity of the laser pulse cancels out. After that, the sign of the slope is reversed after the focus ($z > 2.5$ mm).

Now we consider all possible trajectories tunneled out from every half optical cycle of the driving laser field that contributes to the FTI emission. The phase of the FTI emission shows the asymmetric variation along z (solid black line in figure 1(d)). In addition, it shows the phase modulation due to the interference of the electron wave packets originating from the multiple half optical cycles of the laser field. These phase variations obtained at different target positions is a key parameter to analyze the phase-matching of the FTI emission in a medium.

The FTI emission becomes stronger when the FTI emission generated from individual atoms in the medium are constructively superposed. This phase-matching condition is achieved when the phase variation over the medium length is small. Since the phase slope of the FTI emission is modulated before the focus ($z < 0$), the intensity of the FTI emission can be modulated. The intensity will be strongest right after the focus because the phase variation is minimum. The intensity of the FTI emission can be modulated again after the flat phase region. Note that these predictions for the phase-matching condition are in correspondence with the phase-matching condition of HHG [7, 8].

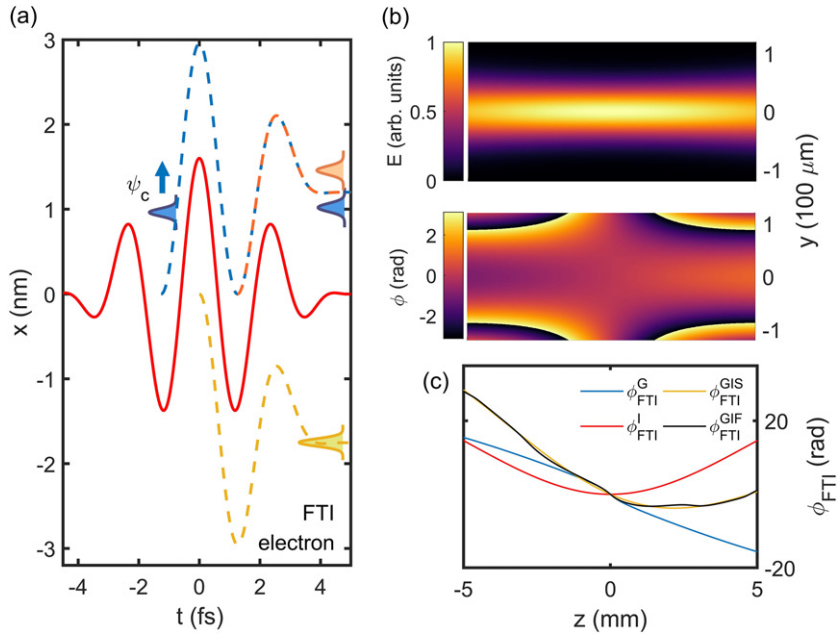

Figure 1. Phase of an FTI emission at different target positions. (a) Classical trajectories of FTI electrons (dashed lines). ψ_c denotes FTI electron wave packet moving along the polarization direction $\boldsymbol{x}$ of a driving laser field after tunneling. The driving laser field is denoted as a solid red line. (b) The amplitude and (c) phase of the driving laser beam with a Gaussian spatial and temporal envelope for the transverse direction $\boldsymbol{y}$ and the propagation direction $\boldsymbol{z}$ (see figure 2 for the definition of $\boldsymbol{x}$, $\boldsymbol{y}$ and $\boldsymbol{z}$). The wavelength is 730 nm, and the beam size is 53 μm in the full-width at half-maximum. (d) The phase of the FTI electron wave packet at different target positions. The solid blue line denotes phase of a single FTI electron trajectory (tunneled at the peak of the laser field) considering the Gouy phase of the laser beam only. The solid red line denotes the phase of the single FTI electron considering the laser intensity only. The solid yellow line denotes the phase of the single FTI electron considering both the Gouy phase and the laser intensity. The solid black line denotes the phase of all FTI electron trajectories considering the Gouy phase and the laser intensity.

2.3. Time-dependent Schrödinger equation

To validate our four-step model, we also solved the time-dependent Schrödinger equation in one spatial dimension (1D TDSE), which can be written as

$$\frac{\partial \psi}{\partial t} = -\frac{1}{2}\frac{\partial^2 \psi}{\partial x^2} + [V(x) + E(t)x]\psi. \tag{1}$$

Here, $\psi = \psi(x, t)$ is electron wavefunction, $V(x) = -1/\sqrt{x^2 + a}$ is soft-core potential in 1D, $E(t)$ is the electric field of a laser pulse. The equation was solved numerically by using the fourth-order Crank–Nicolson scheme. We chose the parameter $a = 0.48$ for the soft core potential to set the ground state binding energy of -24.6 eV which is identical to that of a He atom. Then, we chose the 11th excited state of the soft-core model that yields the FTI emission with a photon energy of 24.2 eV and it corresponds to the FTI emission from the 1s6p state in a He atom.

2.4. Propagation of EUV emission

To compare the FTI emission with the experimental results, the propagation of both the EUV emission and the driving laser field should be carefully taken into account. The EUV emission from individual atoms in the medium can have different phases relative to the driving laser field. This phase-mismatch Δk between the FTI emission and the driving laser field in the medium can be modeled as

$$\Delta k = \Delta k_n + \Delta k_p + \Delta k_g + \Delta k_d. \tag{2}$$

Here, Δk_n, Δk_p, Δk_g, and Δk_d are the phase mismatch caused by the neutral dispersion, the plasma dispersion, the geometric phase variation of the laser beam (i.e., Gouy phase and wavefront curvature), and the intensity-dependent atomic phase accumulated through the FTI trajectory (i.e., ϕ_{FTI}), respectively.

In the experiment, we used a pulsed gas jet with a nozzle diameter of 100 μm which produces a Gaussian density profile with a full width at the half maximum (FWHM) of approximately 250 μm. Since the medium length is short and refractive indices due to the neutral dispersion ($\sim 10^{-5}$) and plasma dispersion ($\sim 10^{-8}$, below 1% ionization) are small, we did not include the neutral and plasma dispersions. This allows us to calculate the far-field spectrum with a few simple steps. First, the FTI emission is

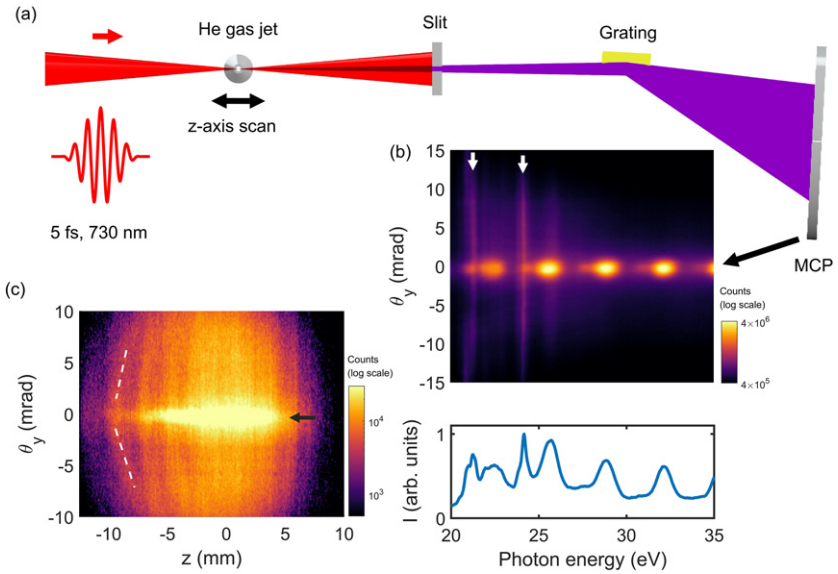

Figure 2. FTI emission obtained at different target positions. (a) Schematic drawing of the experimental setup, top-view. A few-cycle laser pulse (5 fs full-width at half-maximum pulse duration, 730 nm center wavelength) was used to generate high-order harmonics along with EUV line emission generated through FTI. An angle-resolved EUV spectrum was recorded using an imaging microchannel plate (MCP). The helium gas jet was mounted on a translation stage so that the EUV spectrum was recorded at different positions of the gas jet. (b) Angle-resolved EUV spectrum (upper panel) and integrated EUV spectrum (lower panel) recorded in the experiment. Line emissions generated through FTI followed by free induction decay from He 1s2p (21.2 eV) state and He 1s6p (24.2 eV) state are denoted by white arrows. (c) Angle-resolved FTI emission from He 1s6p state obtained at different positions of the gas jet. White dashed lines are guides to the eye. The colormap of the spectrum is normalized for better visualization of the FTI signal. Therefore, the second-order diffraction of the HHG beam at the center indicated by the black arrow is saturated.

calculated using the four-step model or the TDSE model for individual atoms in the medium. When this calculation is made, the intensity and geometrical phase variations of the driving laser field at different positions are considered. Then, the FTI emission is coherently superposed along the propagation direction with a weighting factor for the Gaussian density profile. The FTI emission along the transverse direction is obtained at the near field in this way. Finally, the far-field spectrum is obtained by taking the Fourier transform of the near-field FTI emission along the transverse axis, which can be compared with a spectrum obtained in the experiment.

2.5. Experimental method

To verify the phase variation of the FTI emission near the focus in an experiment, we used a CEP-stabilized, 1 kHz, 30 fs (in the full-width at half-maximum, FWHM), 800 nm Ti:sapphire laser system (Femto laser, Femtopower X pro CEP). The laser pulses were compressed down to a duration of 5 fs (FWHM) using a stretched hollow-core fiber and a set of chirped mirrors. The center wavelength of the few-cycle pulse after the compression was 730 nm. A pulsed gas jet with a nozzle diameter of 100 μm was used to deliver He gas with a backing pressure of 3 bar. The laser beam was focused slightly above the nozzle where the Gaussian-like density profile was measured with the width of 250 μm (FWHM). The pulsed gas jet was operated at the repetition rate of 100 Hz. We recorded angle-resolved EUV spectra using a flat-field EUV spectrometer as shown in figure 2(a). One of the typical angle-resolved EUV spectra recorded in an experiment is shown in figure 2(b). The peak intensity of the laser field at the focus was estimated to be 3.5×10^{14} W cm^{-2} from HHG cutoff energy $\varepsilon_{\mathrm{cutoff}}$ (i.e., $\varepsilon_{\mathrm{cutoff}} = 3.17U_{\mathrm{p}} + I_{\mathrm{p}}$, where U_{p} is the ponderomotive energy of an electron and I_{p} is the ionization potential of the target atom).

3. Results and discussion

3.1. FTI emission

The characteristic features of the FTI emission spectrum are the narrow energy lines and the large divergence angle (upper panel, denoted by white arrows). The line emissions generated through the transition from He 1s2p (21.2 eV, denoted by a white arrow on the left) and He 1s6p (24.2 eV, denoted by a white arrow on the right) to He $1s^2$ are clearly shown in the angle-integrated energy spectrum (figure 2(b), lower panel) as narrow lines. The spectral intensity of the FTI emission of the angle-resolved spectrum is

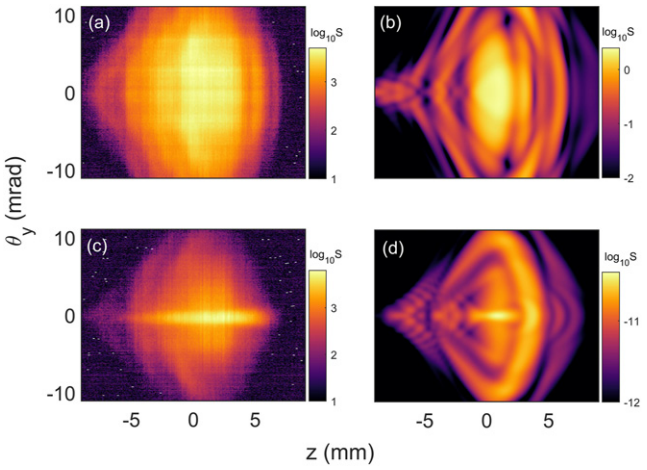

Figure 3. Comparison of FTI emission and HHG at different target positions. (a) Results for FTI emission from He 1s6p to $1s^2$ transition (24.2 eV) obtained in the experiment and (b) TDSE calculations. (c) Results for 17th high-harmonics obtained in the experiment and (d) TDSE calculations. In the TDSE calculations, we chose FTI emission from the 11th excited state, which has transition energy close to 24.2 eV. The medium length was 250 μm.

weak due to the large divergence and the slit in the spectrometer. However, the energy of the FTI beam is comparable to the HHG beam [22].

The spatial distributions of the He 1s6p line emission (24.2 eV) obtained at different target positions are added side by side, as shown in figure 2(c). The bright signal at the center (around $|\theta_y| < 1$ mrad, denoted by black arrow) is the second-order diffraction of high-harmonic radiation, which is commonly observed when a flat-field grating spectrometer is used. The angle-resolved spectra obtained at different positions show an asymmetric distribution. The brightest spectrum is obtained slightly behind the focus ($z = 0$), and the fringe is clear at $z < 0$ while the distribution is smooth at $z > 0$. These experimental observations support the predictions of the four-step model (figure 1(d)) in which the phase of the FTI emission varies rapidly before the focus ($z < 0$), whereas the phase changes slowly after the focus ($z > 0$), supporting the accuracy of the four-step model.

3.2. Long FTI electron trajectory

We compared the spatial distribution of the He 1s6p FTI emission and the 17th harmonic (figures 3(a) and (b)). The spatial distribution of the 17th harmonic is obtained by integrating the spectrum for the energy range from 28.5 to 29.3 eV. Both the FTI emission and the 17th high-harmonic are more intense after the focus ($z > 0$) and show fringes before the focus, which is predicted by the three-step model [8] and the four-step model (figure 1(c)). The HHG spectrum shows two different components as shown in figure 3(b). The bright component at the center corresponds to short-trajectory harmonics. On the other hand, the harmonic emission with a large divergence is produced through long trajectories [29–31]. The large divergence angle of the FTI emission is similar to the high order harmonics generated through long trajectories.

The FTI emission exhibits a large divergence angle, as shown in figure 3(a). This is due to the intensity-dependent phase accumulated along with the long excursion of the electron after tunneling. Unlike HHG, the length of the electron trajectory of the FTI emission is determined by the duration of the driving laser field. For a 5 fs laser pulse, the duration of the FTI trajectory is comparable to the duration of the long trajectory in HHG. The results of numerical calculations obtained by solving the TDSE in 1D are consistent with the experimental results. Although we could not see the detailed structure in the experimental results due to the CEP instability and intensity fluctuation, the overall shape of the spectra is reasonably well reproduced for both FTI emission (figure 3(c)) and HHG (figure 3(d)), supporting our experimental observation.

3.3. Interference of multiple FTI electron trajectories

In order to confirm that the fringes in the angle-resolved FTI spectra are formed due to the interference of electron wave packets generated through multiple electron trajectories, EUV spectra are measured at different target positions for two different CEPs as shown in figure 4. A slow drift of the CEP was stabilized by using an f–2f feedback loop. Although we could not measure the absolute phase of the pulse, we could control the relative CEP by changing the insertion thickness of a pair of fused silica wedges. The difference

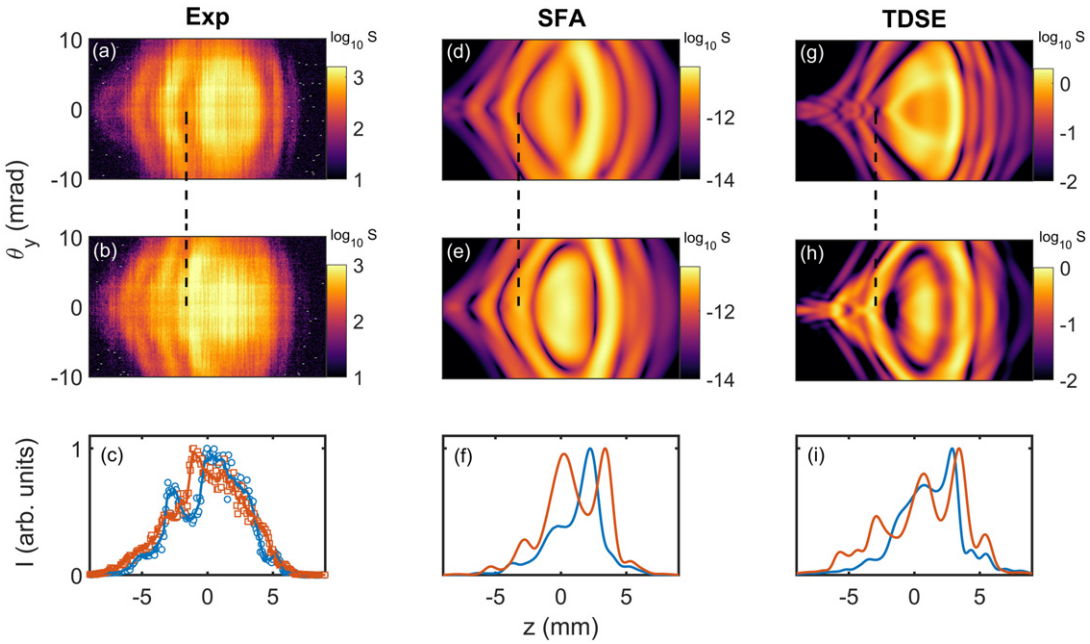

Figure 4. Carrier-envelope phase dependence of FTI emission at different target positions. FTI emissions obtained at different target positions in (a)–(c) experiments, (d)–(f) four-step model calculations, and (g)–(i) TDSE (1D) calculations. The experimental results are obtained at two different CEPs ($\boldsymbol{\Delta\phi_{CEP} = 0.5\pi}$). Vertical dashed lines are drawn to compare the modulation intensity at opposite phases. Similar results were obtained when the calculations were performed by setting the CEPs of $\boldsymbol{0.9\pi}$ [(d) and (g)], and $\boldsymbol{0.4\pi}$ [(e) and (h)]. The third row shows angle-integrated z-axis scan results for the two CEPs. In the third row, solid blue lines correspond to the angle-integrated data shown in the first row, and the solid red lines correspond to the angle-integrated data shown in the second row. Solid lines shown in (c), the experimental data, are smoothed by moving average over five data points, and the corresponding raw data are denoted as markers. In TDSE calculations, the 11th excited state was chosen to match the photon energy of 24.2 eV.

in CEP for the two cases shown in figures 4(a) and (b) was 0.5π. The angle-resolved spectra (figures 4(a) and (b)) show fringes with an opposite phase when the CEP is changed by 0.5π. The angle-integrated signal of experimental results (figure 4(c)) also shows an opposite behavior for the two CEPs in which the peak for one CEP (solid blue lines) changes to the dip for the other CEP (solid red line).

Numerical results were also obtained by solving the four-step model (figures 4(d)–(f)) and TDSE (figures 4(g)–(i)). We obtained the best fit with the experimental results when the CEPs of the driving laser field are 0.4π and 0.9π. While the theoretical calculation shows the interference pattern clearly, the contrast of the interference pattern observed in the FTI spectrum was significantly low. This is because the FTI spectrum was recorded using 100 laser shots. The CEP jitter of the driving laser field (typically 250–500 mrad) degrades the contrast of the interference. Nevertheless, they show a good agreement with the experimental results, as shown in figure 4. Therefore, these experimental observations confirm that the intensity modulation of the FTI spectra is caused by the interference of the electron wave packets created in multiple half optical cycles of the driving laser field.

4. Summary and conclusion

We demonstrated angle-resolved FTI spectra obtained at different target positions and CEPs using few-cycle laser pulses. The angle-resolved FTI spectra exhibit similar behaviors to that of long-trajectory high order harmonics. The angle-resolved FTI spectra show a clear intensity modulation before the focus. The modulation phase changes as we change the CEP of the driving laser pulse. It should be noted that there are fundamental differences in how these intensity modulations are built up. In HHG, the harmonic radiations are emitted at every half optical cycle. The intensity modulation is caused by the interference of the harmonic radiations emitted at the multiple half optical cycles of the driving laser field. On the other hand, the intensity modulation is caused by the coherent superposition of the electron wave packets tunneled out from the multiple half optical cycles of the driving laser field. Therefore, the excitation rate to the excited state is actually modulated. Although the experimental results obtained for HHG and FTI are similar, this fundamental difference should be considered in analyzing the phase response of the FTI emission.

In conclusion, we investigated the phase property of the FTI emission. We compared the spatial distributions of FTI and HHG emissions. We found that the FTI emission is phase-matched after the focus,

showing similar behavior to that of HHG. The FTI emission obtained along with different target positions also shows an intensity modulation similar to that of the long-trajectory HHG. The intensity modulation of the FTI emission obtained at different target positions and CEPs confirms the coherent superposition of the electron wave packet in the excited state. These findings deepen our understanding of the generation mechanism of the FTI emission, which would allow the development of an intense coherent EUV source for applications of photolithography, EUV coherent diffraction imaging, and EUV coherence tomography.

Acknowledgments

This work was supported by the Institute for Basic Science (IBS-R012-D1).

Data availability statement

The data that support the findings of this study are available upon reasonable request from the authors.

ORCID iDs

Yang Hwan Kim https://orcid.org/0000-0001-6504-1856
Igor A Ivanov https://orcid.org/0000-0003-3856-1658
Chang Hee Nam https://orcid.org/0000-0001-8203-0702
Kyung Taec Kim https://orcid.org/0000-0002-5968-8191

References

[1] Ferray M, L'Huillier A, Li X F, Lompre L A, Mainfray G and Manus C 1988 Multiple-harmonic conversion of 1064 nm radiation in rare gases *J. Phys. B: At. Mol. Opt. Phys.* **21** L31
[2] Li X F, L'Huillier A, Ferray M, Lompré L A and Mainfray G 1989 Multiple-harmonic generation in rare gases at high laser intensity *Phys. Rev.* A **39** 5751
[3] Macklin J J, Kmetec J D and Gordon C L 1993 High-order harmonic generation using intense femtosecond pulses *Phys. Rev. Lett.* **70** 766
[4] Corkum P B 1993 Plasma perspective on strong field multiphoton ionization *Phys. Rev. Lett.* **71** 1994
[5] L'Huillier A, Lewenstein M, Salières P, Balcou P, Ivanov M Y, Larsson J and Wahlström C G 1993 High-order harmonic-generation cutoff *Phys. Rev.* A **48** R3433
[6] Lewenstein M, Balcou P, Ivanov M Y, L'Huillier A and Corkum P B 1994 Theory of high-harmonic generation by low-frequency laser fields *Phys. Rev.* A **49** 2117
[7] Lewenstein M, Salières P and L'Huillier A 1995 Phase of the atomic polarization in high-order harmonic generation *Phys. Rev.* A **52** 4747
[8] Salières P, L'Huillier A and Lewenstein M 1995 Coherence control of high-order harmonics *Phys. Rev. Lett.* **74** 3776
[9] Bellini M, Lyngå C, Tozzi A, Gaarde M B, Hänsch T W and L'Huillier A 1998 Temporal coherence of ultrashort high-order harmonic pulses *Phys. Rev. Lett.* **81** 297
[10] Zhou J, Peatross J, Murnane M M, Kapteyn H C and Christov I P 1996 Enhanced high-harmonic generation using 25 Fs laser pulses *Phys. Rev. Lett.* **76** 752
[11] Antoine P, L'Huillier A and Lewenstein M 1996 Attosecond pulse trains using high-order harmonics *Phys. Rev. Lett.* **77** 1234
[12] Chang Z, Rundquist A, Wang H, Murnane M M and Kapteyn H C 1997 Generation of coherent soft x rays at 2.7 nm using high harmonics *Phys. Rev. Lett.* **79** 2967
[13] de Bohan A, Antoine P, Milošević D B and Piraux B 1998 Phase-dependent harmonic emission with ultrashort laser pulses *Phys. Rev. Lett.* **81** 1837
[14] Constant E, Garzella D, Breger P, Mével E, Dorrer C, Le Blanc C, Salin F and Agostini P 1999 Optimizing high harmonic generation in absorbing gases: model and experiment *Phys. Rev. Lett.* **82** 1668
[15] Bartels R, Backus S, Zeek E, Misoguti L, Vdovin G, Christov I P, Murnane M M and Kapteyn H C 2000 Shaped-pulse optimization of coherent emission of high-harmonic soft x-rays *Nature* **406** 164
[16] Kim K T, Zhang C, Ruchon T, Hergott J-F, Auguste T, Villeneuve D M, Corkum P B and Quéré F 2013 Photonic streaking of attosecond pulse trains *Nat. Photon.* **7** 651
[17] Kim K T, Zhang C, Shiner A D, Schmidt B E, Légaré F, Villeneuve D M and Corkum P B 2013 Petahertz optical oscilloscope *Nat. Photon.* **7** 958
[18] Smirnova O, Mairesse Y, Patchkovskii S, Dudovich N, Villeneuve D, Corkum P and Ivanov M Y 2009 High harmonic interferometry of multi-electron dynamics in molecules *Nature* **460** 972
[19] Mairesse Y *et al* 2010 High harmonic spectroscopy of multichannel dynamics in strong-field ionization *Phys. Rev. Lett.* **104** 213601
[20] Shafir D, Soifer H, Bruner B D, Dagan M, Mairesse Y, Patchkovskii S, Ivanov M Y, Smirnova O and Dudovich N 2012 Resolving the time when an electron exits a tunnelling barrier *Nature* **485** 343
[21] Uzan A J *et al* 2020 Spatial molecular interferometry via multidimensional high-harmonic spectroscopy *Nat. Photon.* **14** 188
[22] Yun H, Mun J H, Hwang S I, Park S B, Ivanov I A, Nam C H and Kim K T 2018 Coherent extreme-ultraviolet emission generated through frustrated tunnelling ionization *Nat. Photon.* **12** 620

[23] Nubbemeyer T, Gorling K, Saenz A, Eichmann U and Sandner W 2008 Strong-field tunneling without ionization *Phys. Rev. Lett.* **101** 233001
[24] McKenna J *et al* 2011 Frustrated tunneling ionization during laser-induced D_2 fragmentation: detection of excited metastable D^* atoms *Phys. Rev.* A **84** 043425
[25] Bengtsson S *et al* 2017 Space-time control of free induction decay in the extreme ultraviolet *Nat. Photon.* **11** 252
[26] Amini K *et al* 2019 Symphony on strong field approximation *Rep. Prog. Phys.* **82** 116001
[27] Mun J H, Ivanov I A, Yun H and Kim K T 2018 Strong-field-approximation model for coherent extreme-ultraviolet emission generated through frustrated tunneling ionization *Phys. Rev.* A **98** 063429
[28] Ammosov M V, Delone N B and Krainov V P 1986 Tunnel ionization of complex atoms and of atomic ions in an alternating electromagnetic field *Zh. Eksp. Teor. Fiz.* **91** 2008
[29] Zaïr A *et al* 2008 Quantum path interferences in high-order harmonic generation *Phys. Rev. Lett.* **100** 143902
[30] He L, Lan P, Zhang Q, Zhai C, Wang F, Shi W and Lu P 2015 Spectrally resolved spatiotemporal features of quantum paths in high-order-harmonic generation *Phys. Rev.* A **92** 043403
[31] Lan P *et al* 2017 Attosecond probing of nuclear dynamics with trajectory-resolved high-harmonic spectroscopy *Phys. Rev. Lett.* **119** 033201